A&A 461, 197–204 (2007)
DOI: 10.1051/0004-6361:20064797
© ESO 2006

Astronomy & Astrophysics

VLA NH_3 observations of regions of massive star formation in protostellar cores⋆,⋆⋆

Y. Wang[1,2], Y. Wu[1], Q. Zhang[2], R.-Q. Mao[3], and M. Miller[4]

[1] Astronomy Department and CAS-PKU Joint Beijing Astrophysics Center, Peking University, Beijing 100871, PR China
e-mail: ywang@cfa.harvard.edu
[2] Harvard-Smithsonian Center for Astrophysics, Cambridge, MA 02138, USA
[3] Purple Mountain Observatory, Chinese Academy of Sciences, Nanjing 210008, PR China
[4] I, Physics Institute, Koln Univ., Zulpicher St., 50937 Koln, Germany

Received 1 January 2006 / Accepted 20 August 2006

ABSTRACT

Aims. The high angular resolution images with the Very Large Array (VLA) allow us to explore the general properties of protostellar cores in massive star forming regions at large distances.
Methods. We observed the NH_3 (J, K) = (1, 1) and (2, 2) lines toward five massive protostar candidates (IRAS 18196-1331, IRAS 18352-0148, IRAS 18361-0627, IRAS 18414-0339 and IRAS 19474+2637) with the VLA D configuration.
Results. We found that these objects have hundreds of solar masses in dense gas with rotation temperatures from 8 to 27 K. No 1.3 cm continuum emission was detected at an rms of ~0.7 mJy in all sources except IRAS 18361-0627. We identified 60 clumps and determined their physical parameters (e.g. line width, rotation temperature, size, and mass). The clump masses range from 0.1 $M_\odot$ to 4800 $M_\odot$. The average size, line width and temperature are 0.1 ± 0.06 pc, 1.3 ± 0.4 km s^{-1} and 16 ± 5 K. The discrepancy between NH_3 and (sub)mm continuum emission is found in IRAS 18196-1331. This phenomenon could occur as a result of the NH_3 abundance variation being affected by the UV illumination.

Key words. ISM: clouds – ISM: kinematics and dynamics – stars: formation

1. Introduction

Massive stars ($M > 8\ M_\odot$) are the key ingredients in galaxies. They are responsible for the production of heavy elements and they dominate the evolution of galaxies. The understanding of massive star formation, however, has significantly lagged behind that of low-mass stars. The key missing information is the initial condition for high-mass star formation, largely due to the difficulty of identifying protostellar cores. Because of their rapid evolution, massive protostars are short-lived. Furthermore, the population of massive stars is small. All these aspects make it difficult to obtain core properties at their early evolutionary stages. Since the late 1980's, many studies of high mass star formation targeted ultra compact (UC) HII regions (e.g. Wood & Churchwell 1989; Plume et al. 1992). However, ionization from new born massive stars can alter the parental molecular cloud significantly, leaving little trace of the natal environment during the formation of massive stars.

Over the past decade, there has been a concerted effort to identify high-mass protostellar candidates. One successful approach is to select the IRAS point sources with high flux densities and specific colors that indicate the youth of the objects (e.g. Molinari et al. 1996; Sridharan et al. 2002; Beltran et al. 2005). The selection further requires that no detectable cm emission is associated with the object, thereby filtering out possible HII regions. These studies produced over 100 high-mass protostellar candidates.

We attempted a slightly different approach for identifying high-mass protostellar candidates (Wu et al. 2006) using a sample of IRAS point sources with H_2O maser emission (Comoretto et al. 1990; Brand et al. 1994; Valdettaro et al. 2001). As a signpost of star formation, H_2O masers are found to be associated with the early phases of massive star formation. Similar to other approaches, we further require IRAS flux density >50 Jy and no detection of cm emission. Of 35 objects, we detected dense molecular gas in NH_3 toward 16 sources with the Effelsberg 100 m telescope (Wu et al. 2006).

High-mass protostellar candidates are typically at distances of a few kpc. Single-dish observations in these surveys provide resolutions of 10″−50″, which is not adequate for studying the physical conditions at scales of a few thousand AU around massive young stars. In recent years, high-resolution studies with radio and (sub)mm interferometers revealed disks (e.g. Cesaroni et al. 1997; Zhang et al. 1998, 2002; Beuther et al. 2004) and highly collimated jets (e.g. Cesaroni et al. 1999; Hunter et al. 1999; Beuther et al. 2002). These findings advance our understanding of the formation process of massive stars.

While studies of the individual objects are revealing, high resolution observations of a larger sample are needed to establish general properties of dense molecular gas that gives birth to massive stars. With this in mind, we observed a sample of 5 protostellar candidates with strong NH_3 emission in Wu et al. (2006) with the Very Large Array (VLA). In Sect. 2, we describe the setup of the observations, and in Sect. 3, we present the main

⋆ Table 3, Figs. 3, 6 and 8 are only available in electronic form at http://www.aanda.org

⋆⋆ Figures 2, 4, 5, 7 and 9 are also available in electronic form in FITS format at the CDS via anonymous ftp to cdsarc.u-strasbg.fr (130.79.128.5) or via
http://cdsweb.u-strasbg.fr/cgi-bin/qcat?J/A+A/461/197

Article published by EDP Sciences and available at http://www.aanda.org or http://dx.doi.org/10.1051/0004-6361:20064797

Table 1. Basic properties of the sources in the sample.

Source Name	RA (J2000)	Dec (J2000)	l (°)	b (°)	$L_{\rm bol}$ ($L_\odot$)	D^a (kpc)	Noise (mJy/beam)	Beam size ($'' \times ''$)	PA^b (°)
IRAS 18196-1331	18:22:26.8	–13:30:15	17.638	0.155	6.6×10^4	2.3	2.9	5.71×2.72	–1.67
IRAS 18352-0148	18:37:50.5	–01:45:48	29.811	2.219	5.6×10^3	3.2	2.7	4.80×3.24	29.94
IRAS 18361-0627	18:38:51.7	–06:25:01	25.790	–0.141	5.4×10^4	5.7	2.5	5.00×3.11	28.34
IRAS 18414-0339	18:44:06.9	–03:36:46	28.882	–0.020	2.9×10^4	6.3	2.7	5.00×3.09	32.03
IRAS 19474+2637	19:49:32.6	26:45:14	63.116	0.340	9.7×10^3	2.5	3.2	4.21×3.21	–23.42

Units of right ascension are hours, minutes, and seconds, and units of declination are degrees, arcminutes, and arcseconds.
[a] The kinematic distances (Wu et al. 2006) calculated using the galactic rotation curve (Wouterloot & Brand 1989).
[b] The position angle of the synthesized beam.

results. In Sect. 4, we discuss the physical properties of dense clumps.

2. Observations

We observed the NH_3 (J, K) = (1, 1) line at 23.694 GHz and the (2, 2) line at 23.723 GHz with the VLA of the NRAO[1]. Five sources, IRAS 18196-1331, IRAS 18352-0148, IRAS 18361-0627, IRAS 18414-0339 and IRAS 19474+2637, were observed during June 14–24, 2004 in the compact D configuration. Each source has an on-source integration time of 12 min. We used the 4IF mode that splits the 256-channel correlator into four sections to allow simultaneous observations of the NH_3 (1, 1) and (2, 2) lines with two circular polarizations for each line. The channel separation used was 48.8 KHz (~0.6 km s^{-1} at the line frequency). The bandwidth of 3.13 MHz covers the main and inner-satellite quadrupole hyperfine components. The time variation of the gains was calibrated by quasars observed at a cycle of 20 min. The absolute flux density is established by bootstrapping to 3C 286. The bandpass is calibrated via observations of 3C 273 or 3C 84.

The visibility data sets were calibrated and imaged using the AIPS software package of the NRAO. The average rms of the final images is ~3 mJy/beam per 48.8 KHz wide channel. We also constructed the 1.3 cm continuum emission from the line-free channels in the NH_3 (2, 2) line. The rms in the continuum image is ~0.7 mJy/beam. The angular resolution is about 3″ when using the natural weighting of the visibilities. Table 1 lists the basic parameters of the sources.

According to the VLA website, the typical angular scales that could be missed by the VLA D-array is about 40″–50″. We convolved the VLA images to 40″ resolution (the beam of the Effelsberg 100 m telescope) and compared them with the Effelsberg 100 m data (Wu et al. 2006). We found that VLA images detect 50% to 70% of the single dish flux (IRAS 18352, IRAS 18414, and IRAS 19474 recover ~70%; IRAS 18196 and IRAS 18361 recover about 50%). The missing flux should be extended in nature. When the missing extended emission is scaled to flux per synthesized beam, it amounts to about 3 mJy/beam, comparable to the rms level of the VLA observations. Therefore, the effect of the missing flux on the individual VLA clump mass is small.

[1] The National Radio Astronomy Observatory is operated by Associated Universities, Inc., under cooperative agreement with the National Science Foundation.

Table 2. Physical parameters for five sources.

Source name	Tr^a (K)	τ^b	$FWHM^c$ (km s^{-1})	$N_{\rm Column}$ (10^{21} cm^{-2})	Mass^d ($M_\odot$)
IRAS 18196-1331	9–26	0.01–3.2	0.6–2.5	0.2–22	150
IRAS 18352-0148	9–19	0.01–2.7	0.6–3.1	2.5–82	840
IRAS 18361-0627	8–27	0.01–1.4	0.6–2.2	4.3–31	460
IRAS 18414-0339	8–26	0.05–3.5	0.6–3.7	21–390	6300
IRAS 19474+2637	7–26	0.01–1.7	0.6–3.1	0.4–74	210

[a] Rotation temperature is estimated from the NH_3 (1, 1) and (2, 2) lines. The error in rotation temperature depends on the *S/N* in the spectra. Using the error estimated in Li et al. (2003), we find an error of 0.6 K in rotation temperature toward the emission peaks and 2 K where the *S/N* drops to 3. [b] The error in the optical depth depends on the ratio between the rms noise and the line strength. [c] The velocity resolution and the *S/N* ratio provide the systematic error in *FWHM*. [d] The error in mass is affected by errors in line width and optical depth and, more significantly, the uncertainties in the NH_3 abundance, and source distance.

3. Results

Table 2 lists the physical parameters of the five objects. All five sources (IRAS 18196-1331, IRAS 18352-0148, IRAS 18361-0627, IRAS 18414-0339 and IRAS 19474+2637) have NH_3 emission much higher than 3σ rms (~0.01 Jy). With the kinematic distances (Wu et al. 2006) calculated using the galactic rotation curve (Wouterloot & Brand 1989), we estimate the sizes and masses of NH_3 emissions. The optical depth and rotation temperature are derived following the equations in Ho & Townes (1983). The hydrogen densities depend on the assumption of ammonia fractional abundance, which can vary from 10^{-8} to 10^{-7} according to a study of the Orion molecular cloud (Harju et al. 1993). The preliminary studies in other massive star formation regions (Wu et al. 2006) revealed that the H_2 column density, derived from ammonia column density with abundance of 3×10^{-8}, is lower than the H_2 column density derived from the statistical equation. Thus, we adopted a lower value of $[NH_3]/[H_2] = 10^{-8}$ in our calculation. The derived quantities are listed in Table 2. Columns 1 to 6 show the source name, rotation temperature derived from the NH_3(2, 2) and NH_3(1, 1) lines, the optical depth and line width of the (1, 1) line, the H_2 column density and the mass, respectively.

Since the observations resolved structures in these objects, we give a range of values to several physical parameters. The error in the optical depth depends on the ratio between the rms noise and the line strength. Both the velocity resolution and the *S/N* ratio determine the systematic error in *FWHM*. Rotation temperature is estimated from the NH_3 (1, 1) and (2, 2) lines, and its error in rotation temperature depends on the *S/N* in the NH_3 spectra. Using the error estimate formula in Li et al. (2003), we

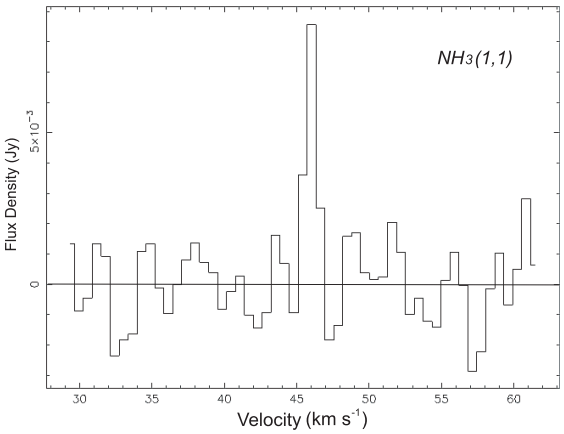

Fig. 1. The NH_3 (1, 1) spectrum for one of the faintest clumps in the IRAS 18352-0148 region. Its position is $\alpha_{(2000)}$ = 18h37m52.1s; $\delta_{(2000)}$ = −1d45m5.4s. The spectrum is spatially smoothed over the size (3.7″) of this clump. The solid line marks the zero level.

find an error of ∼0.6 K in rotation temperature toward the emission peak, and ∼2.5 K where the *S/N* drops to 3. The error in mass is affected by errors in line width and optical depth and, more significantly, by the uncertainties in the NH_3 abundance and source distance.

The NH_3 emissions reveal clumpy structures with many emission peaks. We used the 3D "clfind" program (Williams et al. 1994, 1995) to identify clumps systematically. This algorithm works by first contouring the data at the multiple of the rms noise levels of the observations, then searches for peaks of emission, and follows them down to lower intensities (Williams et al. 1994). This method does not perform any fitting of clumps with a profile. The size and *FWHM* are only calculated via the dispersion. It is designed to be unbiased in that sense and is opposite to gaussclumps (Kramer et al. 1998) in philosophy. Despite the difference in data analysis, the outcome from the two approaches is very similar in practice (Williams et al. 1994). We apply the "clfind" to the channel map and typically set the program to start at 3σ of the rms with intervals of 3σ. Figure 1 shows the NH_3 (1, 1) spectrum from one of the faintest clumps of the IRAS 18352-0148. The emission peak is 9 mJy in the main component and the mass in this clump is only 0.1 $M_\odot$. In this spectrum, the emission appears to be real. However, the optical depth cannot be calculated because the flux in the satellite hyperfine components is below 3σ. Therefore, we assume optically thin emission and use the flux density to derive the column density ($T_B = T_{ex} \cdot \tau$ when optically thin). The column density at an energy level (J, K) does not depend on T_{ex}. The partition function, however, does depend on T_{ex}, which we assume to be similar to the rotation temperature in the nearby area. We refer to the appendix of Mangum et al. (1992) for this calculation. This clump-finding algorithm could overestimate the mass and size for some clumps (Williams et al. 1994). Nevertheless, this quantitative method allows a uniform and an objective way to identify clump, and to compare the clump properties in different regions.

The results of individual sources are given in the sections below.

3.1. IRAS 18196-1331

IRAS 18196-1331, also known as AFGL2136, is in a complex star- formation region with a far infrared luminosity of

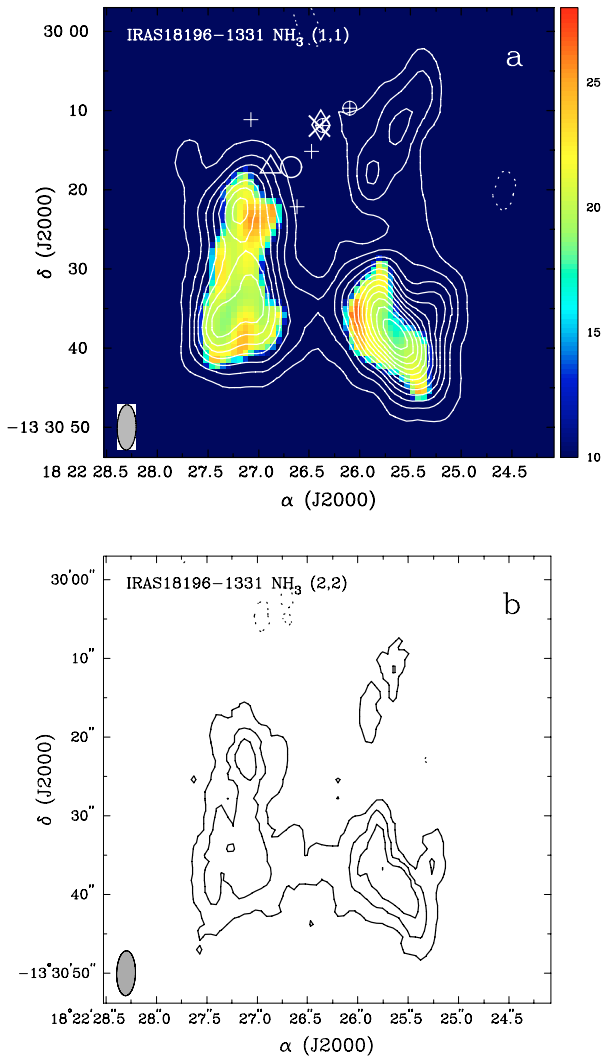

Fig. 2. a) The integrated emission of the NH_3 (1, 1) line in contour for IRAS 18196-1331 overlaid on the rotation temperature color image. The NH_3 emission is contoured at 0.02 Jy beam^{-1} × km s^{-1} intervals starting from 0.01 Jy beam^{-1} × km s^{-1}. The temperature range is from 10 to 28 K. The cross "+" denotes the position of the 2.2 μm point source (Kastner et al. 1992). The "×" sign denotes the position of the 86 GHz emission peak from the OVRO observations (Van de Tak et al. 2000). The triangle denotes the position of the 350 μm emission peak from the CSO observations (Mueller et al. 2002). The circle denotes the position of the 800 μm emission peak from the JCMT observations (Kastner et al. 1994). The diamond denotes the position of water maser detected with the VLA (Menten & Van der Tak 2004). The "⊕" denotes the positions of 0.7 cm continuum sources detected with the VLA (Menten & Van der Tak 2004). **b)** The integrated emission of the NH_3 (2, 2) line. The contour levels are the same as those of the NH_3 (1, 1) line. The synthesized beam is presented in the lower left corner of each image.

6.6 × 10^4 $L_\odot$ at a distance of 2.3 kpc. Its IRAS color is consistent with those of UC HII regions (Wood & Chuchwell 1989). Faint cm emission (lower than 1 mJy beam^{-1} at 6, 3.6 and 2 cm) is detected (Menten & Van der Tak 2004).

Figure 2a presents the image of the integrated NH_3 (1, 1) emission for IRAS 18196-1331 overlaid on the rotation temperature. Figure 2b shows the integrated NH_3 (2, 2) emission. Our NH_3 (1, 1) image from the 100 m single dish telescope shows that the NH_3 (1, 1) emission peak is 40″ away from IRAS 18196-1331. The interferometric observations confirmed

this result and resolved the substructure at high angular resolution. It picks up the more compact structure than the single dish telescope does. In the (1, 1) emission, there appears to be at least 7 large clumps: three toward the east of the region, two clumps toward the southwest of the region, and two toward the northwest along the filament. The NH_3 (2, 2) line emission is weaker than that of the (1, 1) line, but it exhibits structures similar to those in the NH_3 (1, 1) line. The positions of the peak optical depth derived from the main and satellite hyperfine components of the NH_3 (1, 1) line mostly coincide with the emission peaks. The rotational temperature varies from 9 to 26 K in the region. The filament toward the northwest has a temperature range that is lower than 10 K. The local temperature peaks do not always coincide with the peaks of the NH_3 (1, 1) emission, but sometimes appear toward the edges of the clumps. The temperature peak toward the clump to the northeast is close to the dust peak seen at (sub)mm wavelengths (Kastner et al. 1994; Mueller et al. 2002). The heating is likely due to the embedded young star or to shocks from the molecular outflow in the south-north direction (Kastner et al. 1994). On the other hand, the clump to the southwest of the image clearly shows a dip in temperature toward the NH_3 peak, suggesting that no significant internal heating has occurred at the center of this clump.

IRAS 18196-1331 has been studied extensively at other wavelengths. Minchin et al. (1991) report a complex reflection nebula. The 2.2 μm image shows three main lobes (Kastner et al. 1992) nested in the void of the NH_3 emission. Water maser emission was detected at $V_{\rm LSR}$ of 26–27.1 km s^{-1} near the compact 0.7 cm continuum source RS4 at $\alpha_{(2000)}$ = 18h22m26.37s; $\delta_{(2000)}$ = −13d30m11.9s (Menten & Van der Tak 2004). The OVRO 86 GHz continuum image shows an emission peak at a similar position ($\alpha_{(2000)}$ = 18h22m26.4s; $\delta_{(2000)}$ = −13d30m11.9s) (Van de Tak et al. 2000). The CO molecular outflow originating within the cavity of the NH_3 gas extends over 1 pc in the north-south direction (Kastner et al. 1994). The driving source, IRS 1 ($\alpha_{(2000)}$ = 18h22m26.5s; $\delta_{(2000)}$ = −13d30m15s) (Kastner et al. 1994), is very close to the 0.7 cm continuum RS 4 and is probably an evolved massive protostar. It is possible that the high temperature regions toward the edges of the NH_3 emission results from the heating in the interactions of the outflow with the dense molecular gas. We further note that the spatial distribution of the NH_3 emission is different from the (sub)mm continuum emissions. The discrepancy between the NH_3 and dust emission could be caused by the NH_3 abundance variation triggered by the evolved high-mass star(s) in the hole. More detailed discussions will be presented in the following section.

Figure 3 shows the channel maps of the NH_3 (1, 1) main component toward IRAS 18196-1331. There appear to be multiple clumps at different line-of-sight velocities. This is the advantage of using spectral line data that provide kinematic information. The clumps shown in the integrated emission split into many sub-components. Using the quantitative clump identification code (Williams et al. 1994, 1995), we find 14 clumps in the NH_3 (1, 1) emission. The mass, line width, temperature and size are presented in Table 3. For clumps that do not have detectable emission in the (2, 2) line, we compute an upper limit of rotation temperature assuming that the flux density of the (2, 2) line equals to the 3σ level.

3.2. IRAS 18352-0148

IRAS 18352-0148 has a far infrared luminosity of 5.6×10^3 $L_\odot$ at a kinematic distance of 3.2 kpc. No 1.3 cm continuum

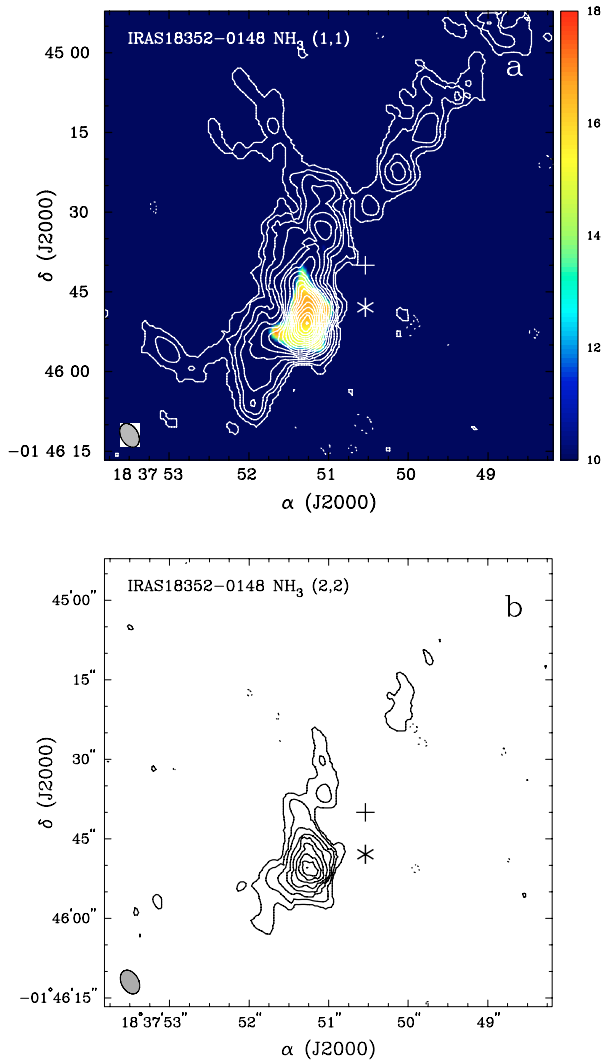

Fig. 4. a) The integrated emission of the NH_3 (1, 1) line for IRAS 18352-0148 overlaid on the rotation temperature color image. The NH_3 emission is contoured at 0.01 Jy beam^{-1} × km s^{-1} intervals starting from 0.005 Jy beam^{-1} × km s^{-1}. The temperature range is from 10 to 18 K. **b)** The integrated NH_3 (2, 2) emission with contour levels the same as the NH_3 (1, 1) line. The cross denotes the position of the MSX point source. The asterisk denotes the position of IRAS 18352-0148. The synthesized beam is presented in the *left corner* of each image.

emission is detected at an rms of 0.7 mJy beam^{-1}, while Fig. 4a presents the image of the integrated emission of the NH_3 (1, 1) overlaid on the rotation temperature. Figure 4b shows the integrated emission of the NH_3 (2, 2) line. The (1, 1) emission shows a filamentary structure extending over 1′ (1 pc) from the southeast to northwest. This component has a temperature of <10 K and a narrow line width of 1.2 km s^{-1}. There is a dominant clump toward the image center. The rotation temperature peaks toward the peak of this clump, indicating internal heating of the clump. The MSX point source G029.8129+02.2195 ($\alpha_{(2000)}$ = 18h37m50.5s; $\delta_{(2000)}$ = −01d45m40s) lies about 15″ to the northwest of the emission peak. Water maser emission has been detected with a $V_{\rm LSR}$ of 43.59 and 43.80 km s^{-1} (Brand et al. 1994), close to the cloud velocity. Both the maser emission and high luminosity indicate that the object is a massive star-forming region.

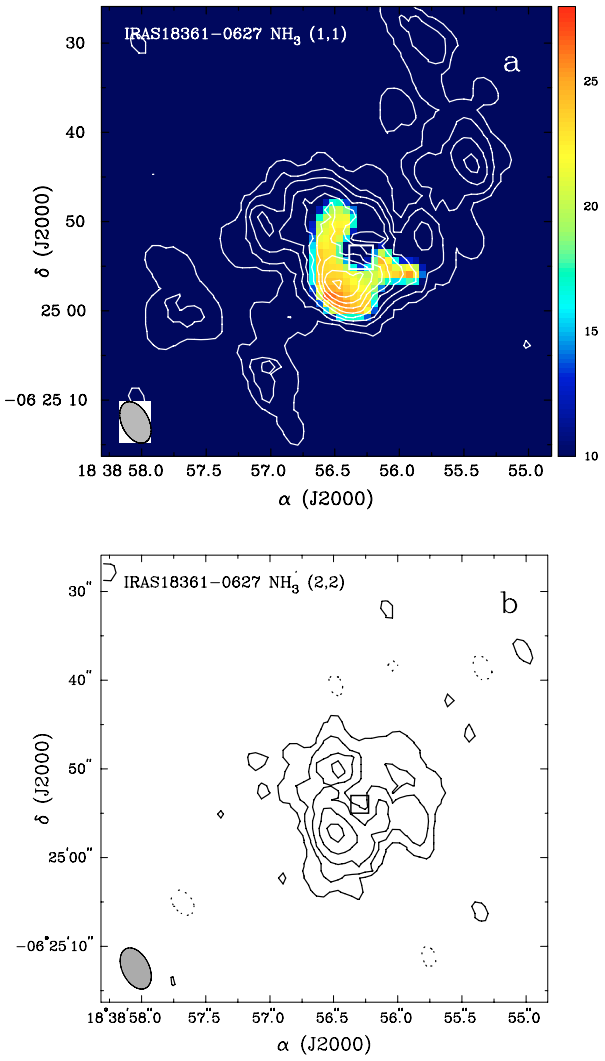

Fig. 5. a) The integrated emission of the NH_3 (1, 1) line for IRAS 18361-0627 overlaid on the rotation temperature color image. The NH_3 emission is contoured at 0.007 Jy beam^{-1} × km s^{-1} intervals starting from 0.01 Jy beam^{-1} × km s^{-1}. The temperature range is from 10 to 28 K. **b)** The integrated NH_3 (2, 2) emission with contour levels the same as the NH_3 (1, 1) line. The square denotes the peak position of the 1.3 cm continuum emission. The synthesized beam is presented in the *lower left corner* of each image.

Using the clump identification algorithm, we found 10 clumps in this region. The largest clump contains a mass of 600 $M_\odot$, a rotation temperature of 16 K, and a line width of 1.8 km s^{-1}. The mass, line width, temperature, and size are presented in Table 3.

3.3. IRAS 18361-0627

IRAS 18361-0627 has a far infrared luminosity of 5.4 × 10^4 $L_\odot$ at a distance of 5.7 kpc. The NH_3 peak obtained with the Effelsberg 100 m telescope is about 1.5′ offset from IRAS 18361-0627, but coincides with an MSX point source (Wu et al. 2006). An unresolved continuum source at 1.3 cm is detected toward this region, with a peak flux density of 25 mJy/beam ($\alpha_{(2000)}$ = 18h38m56.3s; $\delta_{(2000)}$ = −06d24m54s). Figure 5a presents the image of the integrated emission of the NH_3 (1, 1) line overlaid on the rotation temperature, while Fig. 5b shows the integrated emission of the NH_3 (2, 2) line. Figure 6 presents the channel maps of the main hyperfine component of the NH_3 (1, 1) line. Both the (1, 1) and (2, 2) emissions show a partial shell structure surrounding the 1.3 cm continuum source. This shell structure is also seen at the V_{LSR} of 94.8 km s^{-1} in the channel maps (Fig. 6). The temperature derived from the (1, 1) and (2, 2) lines highlights a similar shell structure with temperatures varying from 15 to 28 K. The highest temperature region is located toward the tip of the bow near the NH_3 (1, 1) emission peaks. The position of the 1.3 cm continuum is offset from the NH_3 (1, 1) and (2, 2) peaks. This UCHII region has probably triggered photochemistry that enhances the NH_3 gas emission around the HII region (Viti & Williams 1999). The clumps of the NH_3 (1, 1) traces the cold material that is currently forming stars. And the shell-like structure may indicate star formation trigged by the UCHII region.

We identified 16 clumps in the NH_3 (1, 1) emission. The most massive one is located at the NH_3 (1, 1) emission peak with 110 $M_\odot$. The rotation temperature of the most massive clump is 23 K and the line width is 1.5 km s^{-1} (see Table 3). The temperatures of the clumps vary from a few K to 23 K, and line widths change from 0.6 to 1.7 km s^{-1}. The mass, line width, temperature, and size of the clumps are listed in Table 3.

3.4. IRAS 18414-0339

IRAS 18414-0339 has a far infrared luminosity of 2.9 × 10^4 $L_\odot$ at a distance of 6.3 kpc. No 1.3 cm continuum emission is detected at an rms of 0.7 mJy beam^{-1}, and Fig. 7a presents the integrated emission of the NH_3 (1, 1) line overlaid on the rotation temperature. Figure 7b shows the integrated emission of the NH_3 (2, 2) line. The NH_3 emission shows a compact clump toward the center of the image, surrounded by an extended envelope in the east-west direction.

Figure 8 presents the channel maps of the main hyperfine component of the NH_3 (1, 1) line. There appears to be a velocity gradient from the northwest to southeast. The emission lies in the northwest at 99.2 km s^{-1} and in the southeast at 103.5 km s^{-1}. There is a high temperature (20–27 K) bar extended from the northeast to southwest, perpendicular to the direction of the velocity gradient. The MSX point source, G028.8829-00.0191, is about 7″ away from the NH_3 emission peak. Considering the position error of MSX 8 μm data (∼5″), the MSX source could be associated with the emission peak. The peaks of the rotation temperature indicate internal heating from the embedded protostar(s).

In addition, the line wings toward the emission peak extend to 6 km s^{-1}. The large line width in the emission peak indicates unresolved motions (3″ is equivalent to ∼0.1 pc at the distance of 6.3 kpc) in the gas, similar to the case in IRAS 20126+4104 (Zhang et al. 1998), AFGL 5142 (Zhang et al. 2002) and IRAS 18566+0408 (Zhang et al. 2006). We suggest that there might be a massive rotating toroid toward the emission peak surrounded by an envelope with a small velocity gradient. On the other hand, the large line width can also be due to spatially unresolved clumps with different velocities. Follow-up observations are needed to confirm the interpretation.

We identified 5 clumps in the region. The most massive clump has a mass of 4800 $M_\odot$ and a rotation temperature of 20 K. The line width of 2.6 km s^{-1} is much larger than the 1 km s^{-1} *FWHM* in the extended envelope and the thermal line width of gas at 20 K. The mass, line width, temperature, and size of the clumps are listed in Table 3.

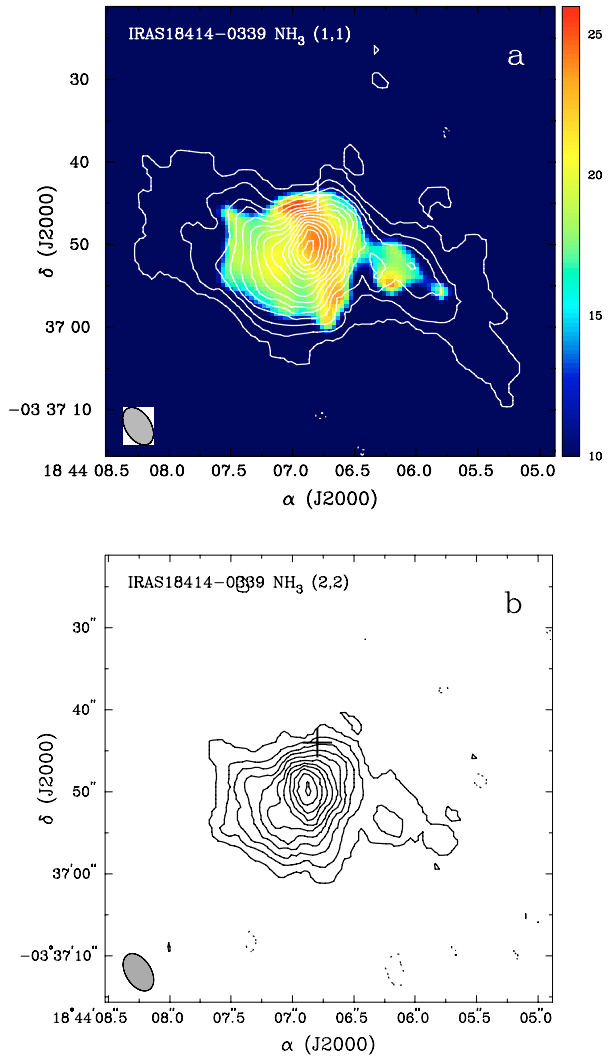

Fig. 7. a) The integrated emission of the NH_3 (1, 1) line for IRAS 18414-0339 overlaid on the rotation temperature color image. The NH_3 emission is contoured at 0.002 Jy beam^{-1} × km s^{-1} intervals starting from 0.001 Jy beam^{-1} × km s^{-1}. The temperature range is from 10 to 26 K. **b)** The integrated NH_3 (2, 2) emission with contour levels the same as the NH_3 (1, 1) line. The cross denotes the position of the MSX point source (G028.8829-00.0191). The synthesized beam is presented in the *lower left corner* of each image.

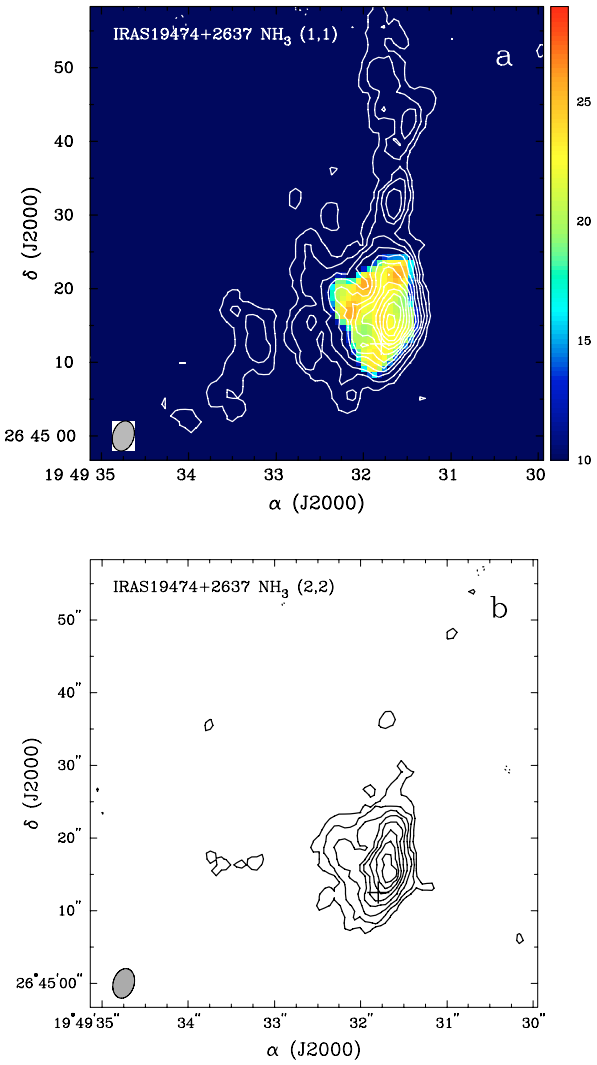

Fig. 9. a) The integrated emission of the NH_3 (1, 1) line for IRAS 19474+2637 overlaid on the rotation temperature color image. The NH_3 emission is contoured at 0.014 Jy beam^{-1} × km s^{-1} intervals starting from 0.007 Jy beam^{-1} × km s^{-1}. The temperature range is from 10 to 29 K. **b)** The integrated NH_3 (2, 2) emission with contour levels the same as the NH_3 (1, 1) line. The cross denotes the position of the MSX point source. The synthesized beam is presented in the lower left corner of each image.

3.5. IRAS 19474+2637

IRAS 19474+2637 has a far infrared luminosity of 9.7×10^3 $L_\odot$ at a distance of 2.5 kpc. No 1.3 cm continuum emission is detected at an rms of 0.7 mJy beam^{-1}. The integrated emission of the NH_3 (1, 1) line in Fig. 9a shows a dominant peak associated with the MSX point source G063.1140+00.3416 (19h49m32.0s; +26d45m12.1s). The emission is elongated along the north-south direction. There appears to be a steep drop off in the flux density toward the west of the emission peak. The NH_3 (2, 2) emission is weaker, but it shows structures similar to those of the NH_3 (1, 1) line (Fig. 9b).

We identified 15 clumps in the filament. The most massive clump toward the emission peak has a mass of 57 $M_\odot$, a rotation temperature of 22 K, and a line width of 1.7 km s^{-1}. The temperature image shows 4 high temperature regions close to the peak of the clumps. They are probably heated internally by protostars. The mass, line width, temperature, and size of the clumps are listed in Table 3.

4. Discussions

4.1. General properties

With the high-angular resolution images obtained from the VLA, it is possible to study the properties of the clumps in massive star-formation regions at large distances. We identified 60 clumps in 5 regions. Tables 3 lists the parameters of clumps above the detection limit (5σ rms) for each region. Columns 1 to 10 indicate the source name, RA (2000), Dec(2000), velocity in the emission peak, the peak flux density, size, line width of the (1, 1) line, rotation temperature, mass, and virial mass, in that order. The rotation temperature is the average value in each clump. For clumps that do not have detectable emission in the (2, 2) line, an upper limit for the rotation temperature

is given. The virial mass is obtained using the relation, $M_{\rm vir} = 105(D/{\rm pc})(\Delta V/{\rm km\,s^{-1}})^2(M_\odot)$, following Estalella et al. (1993), where D is the diameter of this clump and ΔV its line width. Other parameters are derived from the clump-find code. The clump masses range from 0.1 $M_\odot$ to 4800 $M_\odot$. For the 60 clumps, the average ratio of $M/M_{\rm vir}$ is 0.67, with a range from ~0.01 to 10. The large variation in the ratio suggests that the NH_3 abundance may vary from region to region. On the other hand, most low-mass clumps (<10 $M_\odot$) in each region have $M_{\rm vir}$ much larger than M. These clumps could be the unvirialized transient structures. The more massive clumps (>10 $M_\odot$) have comparable $M_{\rm vir}$ and M, except for the most massive clump in IRAS 18414-0339 with $M \gg M_{\rm vir}$. Due to the uncertainty of the NH_3 abundance, the dynamic status of these clumps cannot be reliably constrained so require further investigation.

The average size, line width and temperature are 0.1 ± 0.06 pc, 1.3 ± 0.4 km s^{-1}, and 16 ± 5 K. The error bar here represents the standard deviation in the data. It appears that the average line width is narrower than that from the observations with the Effelsberg 100 m telescope (Wu et al. 2006; Sridharan et al. 2002; Molinari et al. 1996). The larger line width from the single- dish data could be due to the broadening of unresolved motions within the large beam. The average rotation temperature of 16 K is lower than the temperature of 19 K from Wu et al. (2006) and 18.5 K based on other single-dish observations (Sridharan et al. 2002; Molinari et al. 1996). The temperature from the single-dish observations is a flu-density weighted average over the 40″ beam. On the contrary, the average temperature from the VLA weights all the clumps equally. This may explain the lower average clump temperature in the VLA observations.

4.2. The discrepancy between NH_3 and dust emission

Because of chemical variations in dense cores, the emissions of different gas tracers and dust may appear different. As shown in Sect. 3.1, e.g. IRAS 18196-1331, the distribution of the NH_3 emission in some cases differs from that of dust. The NH_3 (1, 1) image obtained from the VLA shows a ring-like structure surrounding the peak of the dust continuum emission obtained from OVRO (Fig. 2a). The dust emission peak coincides with the cm continuum emission indicating that it contains more evolved high-mass star(s). Furthermore, similar to the cm and mm peaks, the near-infrared point sources (Kastner et al. 1992; Menten & Van der Tak 2004) also reside in the void of the NH_3 emission. Therefore, the ring-like NH_3 emission could represent a remnant envelope in the act of dispersal due to the star forming activities, such as outflow, jet and stellar wind.

The ring-like NH_3 emission toward IRAS 18196-1331 can also be caused by the UV-triggered photochemistry (Viti & Williams 1999; Girart et al. 1994). The theoretical model proposed by Taylor & Williams (1996) predicts that the UV illumination can evaporate the ice mantles, such as NH_3, on dust grains. As a result, the NH_3 abundance is enhanced in these regions. A similar phenomenon is found in Herbig-Haro (HH) objects (Girart et al. 1994; Tieftrunk et al. 1998). Shocks produced by a jet from a protostar generate the UV radiation that illuminates the density enhancement in the vicinity. This process enhances the NH_3 and HCO^+ abundance often observed near the HH objects. Our NH_3 VLA image shows that the molecular line emission surrounds the massive outflows generated by the IRS1. The evaporation could occur as a result of UV illumination from both the shocks generated by the massive outflow and the evolved massive stars in the hole. On the other hand, the UCHII region in the hole has probably dispersed the gas envelope which leads to not detecting of NH_3 even though there are UV photons (Zinchenko et al. 1998; Wu et al. 2006; Shepherd et al. 2004). The OVRO 3.4 mm emission may come from a circumstellar disk around IRS1 that is so compact as to be smeared in the single-dish continuum imaging. The NH_3 is not expected in this region that is so close to the star where the NH_3 could be destroyed by a chemical reaction with carbon ion (Turner et al. 1995).

Considering the offset between 1.3 cm continuum and NH_3 emission in IRAS 18362-0627, a similar process could also happen there. Both chemical and physical effects on the NH_3 abundance may contribute to the complexity in high-mass star-formation regions and give rise to the difference between the dust and the NH_3 emission. More comparative studies of NH_3 and (sub)mm continuum emission, in conjunction with other molecular tracers are needed to further resolve the difference.

5. Summary

We imaged five massive protostar candidates (IRAS 18196-1331, IRAS 18352-0148, IRAS 18361-0627, IRAS 18414-0339 and IRAS 19474+2637) with the VLA in the NH_3 (1, 1) and (2, 2) lines at high angular resolution. The molecular gas in these regions shows clumpy structures. Applying the 3D clump-find algorithm (Williams et al. 1994), we identified 60 clumps in the whole sample. The masses of these clumps range from 0.1 $M_\odot$ to 4800 $M_\odot$. The average size, line width and rotation temperature in the regions are 0.1 ± 0.06 pc, 1.3 ± 0.4 km s^{-1}, and 16 ± 5 K. In addition, we found that in the presence of more evolved high-mass stars in the region, the NH_3 and (sub)mm emission may not trace each other due to UV-triggered chemistry and/or the dispersal of the dense molecular core.

Acknowledgements. We would like to thank Yuan Chen for her comments in data reduction and analysis. We also would like to acknowledge helpful conversations with Paul Ho, Luis Zapata and Junzhi Wang. We acknowledge enlightening comments from an anonymous referee. This research is supported by the Grants 10128306, 110133020, 10203003, 10373025 of NSFC and G1999075405 of NKBRSF.

References

Adams, F. C., & Fattuzzo, M. 1996, ApJ, 464, 256
Aikawa, Y., Ohashi, N., & Herbst, E. 1996, ApJ, 593, 906
Beltran, M., Brand, J., Cesaroni, R., et al. 2006, A&A, 447, 221
Beuther, H., & Schilke, P. 2004, Science, 303, 1167
Beuther, H., Schilke, P., Sridharan, T. K., et al. 2002, A&A, 383, 892
Bonnell, I. A., Bate, M. R., Clarke, C. J., & Pringle, J. E. 1997, MNRAS, 285, 201
Bonnell, I. A., Bate, M. R., & Zinnecker, H. 2001, MNRAS, 324, 573
Bonnell, I. A., Bate, M. R., & Zinnecker, H. 2004, MNRAS, 349, 735
Bonnor, W. G. 1956, MNRAS, 116, 351
Brand, J., Cesaroni, R., Caselli, P., et al. 1994, A&AS, 103, 541
Carey, S. J., Clark, F. O., Egan, M. P., et al. 1998, ApJ, 508, 721
Cesaroni, R., Felli, M., Testi, L., Walmsley, C. M., & Olmi, L. 1997, A&A, 325, 725
Cesaroni, R., Felli, M., Jenness, T., et al. 1999, A&A, 345, 949
Codella, C., Palumbo, G. G. C., Pareschi, G., et al. 1995, MNRAS, 276, 57
Egan, M. P., Shipman, R. F., Price, S. D., et al. 1998, ApJ, 494, L199
Elmegreen, B. G. 1997, ApJ, 486, 944
Elmegreen, B. G., & Falgarone, E. 1996, ApJ, 471, 816
Estalella, R., Mauersberger, R., Torrelles, J. M., et al. 1993, ApJ, 419, 698
Gammie, C. F., Lin, Y., Stone, J. M., & Ostriker, E. C. 2003, ApJ, 592, 203
Girart, J. M., Rodriguez, L. F., Anglada, G., et al. 1994, ApJ, 435, L145
Goodman, A. A., Barranco, J. A., Wilner, D. J., & Heyer, M. H. 1998, ApJ, 504, 223
Harju, J., Walmsley, C. M., & Wouterloot, J. G. A. 1993, A&AS, 98, 51
Ho, P. T. P., & Townes, C. H. 1983, A&AR, 35, 239
Hotzel, S., Harju, J., & Walmsley, C. M. 2004, A&A, 415, 1065
Hunter, T. R., Testi, L., Zhang, Q., & Sridharan, T. K. 1999, AJ, 118, 477

Kramer, C., Stutzki, J., Rohrig, R., & Corneliussen, U. A. A. 1998, 329, 249
Kastner, J. H., Weintraub, D. A., & Aspin, C. 1992, ApJ, 389, 357
Kastner, J. H., Weintraub, D. A., Snell, R. L., Sandell, G., & Aspin, C. 1994, ApJ, 425, 695
Kerton, C. R., Martin, P. G., Johnstone, D., & Ballantyne, D. R. 2001, ApJ, 552, 601
Li, D., Goldsmith, P. F., & Menten, K. 2003, ApJ, 587, 262
Mangum, J. G., Wootten, A., & Mundy, L. G. 1992, ApJ, 388, 467
McLaughlin, D. E., & Pudritz, R. E. 1996, ApJ, 469, 194
Menten, K. M., & Van der Tak, F. F. S. 2004, A&A, 414, 289
Minchin, N. R., Hough, J. H., Burton, M. G., & Yamashita, T. 1991, MNRAS, 251, 522
Miralles, M., Rodriguez, L., & Scalise, E. 1994, ApJS, 92, 173
Molinari, S., Brand, J., Cesaroni, R., & Palla, F. 1996, A&A, 308, 573
Mookerjea, B., Kramer, C., Nielbock, M., & Nyman, L. 2004, A&A, 426, 119
Mueller, K. E., Shirley, Y. L., Evans II, N. J., & Jacobson, H. 2002, A&AS, 143, 469
Myers, P. C. 1998, ApJ, 496, L109
Padoan, P., & Nordlund, A. 2002, ApJ, 576, 870
Pillai, T., Wyrowski, F., Menten, K. M., & Krügel, E. 2006, A&A, 450, 569
Plume, R., Jaffe, D. T., & Evans II, N. J. 1992, ApJS, 78, 505
Rathborne, J. M., Jackson, J. M., Chambers, E. T., et al. 2005, ApJ, 630, L181
Reid, M. A., & Wilson, C. D. 2005, ApJ, 625, 891
Sridharan, T. K., Beuther, H., Schilke, P., Menten, K. M., & Wyrowski, F. 2002, ApJ, 566, 931
Shepherd, D. S., Borders, T., Claussen, M., Shirley, Y., & Kurtz, S. 2004, ApJ, 614, 211
Tafalla, M., Mardones, D., Myers, P. C., et al. 1998, ApJ, 504, 900
Tafalla, M., Myers, P. C., Caselli, P., Walmsley, C. M., & Comito, C. 2002, ApJ, 569, 815
Taylor, S. D., & Williams, D. A. 1996, MNRAS, 282, 1343
Tieftrunk, A. R., Megeath, S. T., Wilson, T. L., & Rayner, J. T. 1998, A&A, 336, 991
Tilley, D. A., & Pudritz, R. E. 2004, MNRAS, 353, 769
Tothill, N. F. H., White, G. J., Matthews, H. E., et al. 2002, ApJ, 580, 285
Valdettaro, R., Palla, F., Brand, J., et al. 2001, A&A, 368, 845
Van der Tak, F. F. S., Van Dishoeck, E. F., Evans, N. J., II, & Blake, G. A. 2000, ApJ, 537, 283
Wang, Y., Zhang, Q., Thushara, G. S., et al., in preparation
Williams, J. P., De Geus, E. J., & Blitz, L. 1994, ApJ, 428, 693
Williams, J. P., Blitz, L., & Stark, A. A. 1995, ApJ, 451, 252
Williams, S. J., Fuller, G. A., & Sridharan, T. K. 2004, A&A, 417, 115
Wood, D. O. S., & Churchwell, Ed 1989, ApJ, 340, 265
Wouterloot, J. G. A., & Brand, J. 1989, A&AS, 80, 149
Wu, Y., Zhang, Q., Yu, W., et al. 2006, A&A, 450, 607
Zhang, Q., Hunter, T. R., & Sridharan, T. K. 1998, ApJ 505, 151
Zhang, Q., Hunter, T. R., Sridharan, T. K., & Ho, P. T. P. 2002, ApJ, 566, 982
Zhang, Q., et al. 2005, submitted
Viti, S., & Williams, D. A. 1999, MNRAS, 310, 517
Zinchenko, I., Pirogov, L., & Toriseva, M. 1998, A&AS, 133, 337

Online Material

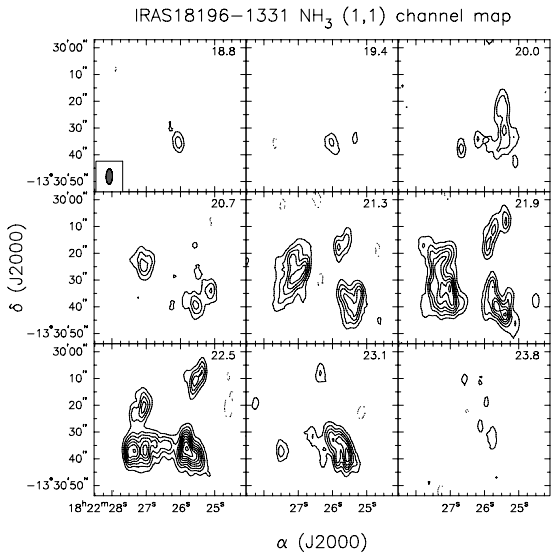

Fig. 3. The channel maps of the NH_3 (1, 1) main hyperfine component for IRAS 18196-1331. The contours are drawn at 3σ intervals (1σ = 0.0033 Jy beam^{-1}) starting from 3σ. The pointing center is [0″, −40″] offset from the IRAS 18196-1331 position. The synthesized beam is presented in the *lower left corner of the first panel*.

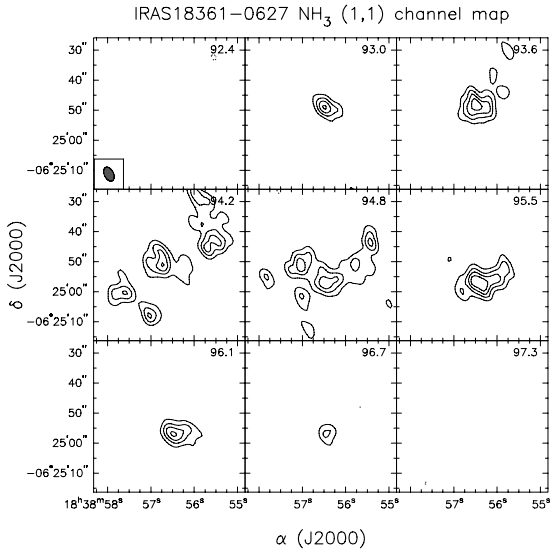

Fig. 6. The channel maps of the NH_3 (1, 1) main hyperfine component for IRAS 18361-0627. The contours are drawn at 3σ intervals (1σ = 0.0025 Jy beam^{-1}) starting from 3σ. The pointing center is [80″, 0″] offset from IRAS 18361-0627. The synthesized beam is presented in the *lower left corner of the first panel*.

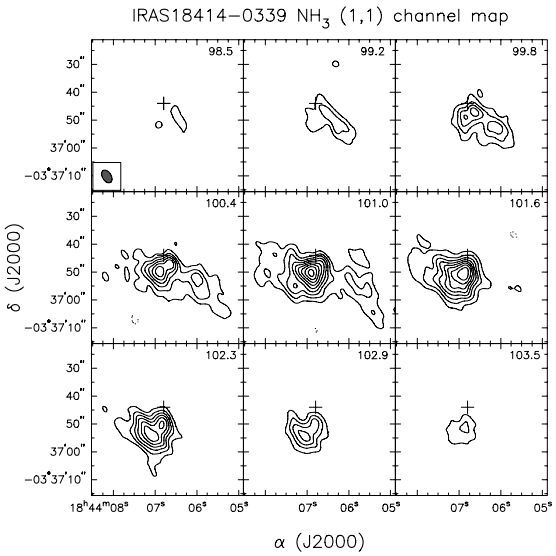

Fig. 8. The channel maps of the NH_3 (1, 1) main hyperfine component for IRAS 18414-0339. The contours are drawn at 3σ intervals (1σ = 0.0027 Jy beam^{-1}) starting from 3σ. The cross denotes the position of the MSX point source (G028.8829-00.0191). The synthesized beam is presented in the *lower left corner of the first panel*.

Table 3. Physical parameters of individual clumps.

Source name	RA (J2000)	Dec (J2000)	υ_{peak} (km s^{-1})	T_{peak} (K)	Size[a] ($''$)	*FWHM*[a] (km s^{-1})	Tr[b] (K)	Mass ($M_\odot$)	Virial mass ($M_\odot$)
IRAS 18196−1331	18:22:25.8	−13:30:35.8	22.5	0.09	6.4	2.0	21	43	60
	18:22:27.0	−13:30:33.4	21.9	0.07	4.8	1.1	21	6.1	14
	18:22:27.3	−13:30:37.4	22.5	0.07	6.5	1.1	21	4.3	18
	18:22:25.4	−13:30:43.0	21.9	0.06	6.2	1.9	20	19	53
	18:22:26.9	−13:30:26.2	21.3	0.05	8.0	1.5	22	9.3	42
	18:22:25.6	−13:30:11.0	22.5	0.05	6.2	1.2	<9.5	0.5	21
	18:22:27.5	−13:30:32.6	21.9	0.05	6.8	1.2	21	0.1	23
	18:22:25.2	−13:30:35.0	21.3	0.05	4.6	2.0	19	3.2	43
	18:22:26.7	−13:30:34.2	22.5	0.05	4.5	1.1	22	0.4	13
	18:22:25.4	−13:30:31.0	20.0	0.03	4.8	2.6	22	6.6	76
	18:22:25.9	−13:30:17.4	21.9	0.03	4.4	1.4	<12	17	20
	18:22:26.7	−13:30:37.4	20.0	0.03	3.9	0.6	21	0.5	3
	18:22:26.1	−13:30:35.0	18.8	0.03	4.5	1.4	23	5.3	21
	18:22:25.9	−13:30:19.0	23.8	0.01	3.5	1.9	<11	20	30
IRAS 18352−0148	18:37:51.3	−1:45:50.4	44.8	0.08	15	1.8	16	600	160
	18:37:51.0	−1:45:30.9	45.4	0.03	6.0	1.8	17	100	64
	18:37:50.1	−1:45:22.4	46.0	0.03	7.3	1.4	<13	8.7	47
	18:37:49.8	−1:45:14.9	46.0	0.03	7.1	1.0	<10	4	23
	18:37:53.0	−1:45:56.4	46.0	0.02	4.9	0.8	<9.6	1.8	10
	18:37:51.7	−1:45:12.9	46.0	0.02	5.8	0.7	<13	0.3	9
	18:37:49.2	−1:45:5.90	47.3	0.02	6.1	1.9	<13	0.3	72
	18:37:52.7	−1:45:59.9	46.6	0.01	8.2	1.7	<14	6.2	77
	18:37:52.1	−1:45:5.40	46.0	0.01	3.7	0.6	<15	0.1	4
	18:37:51.4	−1:45:19.9	46.0	0.01	8.4	1.7	<15	40	79
IRAS 18361−0627	18:38:56.4	−6:24:57.5	95.5	0.05	6.0	1.6	23	32	89
	18:38:56.5	−6:24:47.9	93.6	0.05	5.5	1.2	21	92	46
	18:38:56.7	−6:24:51.1	94.2	0.04	4.1	1.7	22	81	69
	18:38:57.1	−6:24:51.1	94.8	0.04	5.2	0.8	<14	23	19
	18:38:55.7	−6:24:45.5	94.2	0.04	4.3	1.1	<11	0.5	30
	18:38:55.5	−6:24:43.1	94.2	0.03	5.2	0.8	<12	0.8	19
	18:38:57.0	−6:25:7.90	94.2	0.03	4.5	0.8	<12	0.6	17
	18:38:57.6	−6:25:0.70	94.2	0.03	5.2	0.6	<12	13	11
	18:38:55.9	−6:24:27.9	94.2	0.03	4.9	0.6	<11	0.7	10
	18:38:55.8	−6:24:51.9	95.5	0.03	5.9	1.5	23	110	77
	18:38:57.8	−6:24:55.1	94.8	0.02	3.8	0.7	<8.9	11	11
	18:38:57.0	−6:25:1.50	94.8	0.02	3.5	0.8	<13	0.4	13
	18:38:56.8	−6:24:59.9	95.5	0.02	3.6	1.0	24.5	0.5	21
	18:38:54.6	−6:25:6.30	93.6	0.02	3.4	0.6	<13	0.3	7
	18:38:56.0	−6:24:37.5	94.2	0.02	4.6	0.7	<13	0.6	13
	18:38:55.3	−6:24:35.1	94.2	0.01	4.1	0.6	<8.9	0.5	9
IRAS 18414−0339	18:44:6.9	−3:36:50.4	101.0	0.09	11	2.6	20	4800	480
	18:44:6.0	−3:36:52.4	100.4	0.04	7.7	1.8	18	540	160
	18:44:5.4	−3:37:4.40	101.0	0.02	6.4	1.0	<9.5	44	41
	18:44:7.8	−3:36:43.9	101.0	0.02	9.1	1.5	19	300	132
	18:44:5.8	−3:36:44.9	101.0	0.02	5.5	1.2	<8.9	1.1	51
IRAS 19474+2637	19:49:31.7	26:45:13.9	20.4	0.07	6.3	1.7	22	57	46
	19:49:31.6	26:45:18.7	18.6	0.07	4.4	1.9	22	39	41
	19:49:32.2	26:45:19.5	21.0	0.06	5.1	1.4	22	15	26
	19:49:31.8	26:45:21.9	19.8	0.05	4.7	2.0	23	29	48
	19:49:31.6	26:45:31.5	19.2	0.04	4.5	1.3	<13	1.0	19
	19:49:33.1	26:45:12.3	20.4	0.03	4.3	1.2	<12	0.8	16
	19:49:32.7	26:45:14.7	21.0	0.03	5.5	1.1	<9.4	1.2	17
	19:49:31.4	26:45:44.3	18.6	0.03	3.3	1.2	<12	0.4	12

Table 3. continued.

Source name	RA (J2000)	Dec (J2000)	υ_{peak} (km s^{-1})	T_{peak} (K)	Size[a] ($''$)	*FWHM*[a] (km s^{-1})	Tr[b] (K)	Mass ($M_\odot$)	Virial mass ($M_\odot$)
	19:49:31.9	26:45:49.9	17.3	0.03	4.4	1.9	<7.8	1.1	41
	19:49:31.7	26:45:47.5	19.2	0.03	3.9	1.1	<8.6	0.4	12
	19:49:31.8	26:45:37.9	19.2	0.02	3.4	1.2	<13	0.4	12
	19:49:32.4	26:45:29.9	19.8	0.02	2.4	0.8	<13	0.1	4.0
	19:49:33.4	26:45:9.90	19.8	0.02	4.5	0.7	<13	0.3	6.0
	19:49:32.7	26:45:25.9	20.4	0.02	3.6	0.9	<13	0.2	7.0
	19:49:31.5	26:45:42.7	19.8	0.02	3.0	1.9	<13	0.4	28

Units of right ascension are hours, minutes, and seconds, and units of declination are degrees, arcminutes, and arcseconds. The incompleteness mass threshold is 0.1 $M_\odot$. The sizes and line widths are corrected for resolution.

[a] The size and *FWHM* are corrected by the beam size and velocity resolution, respectively (Williams et al. 1994). These parameters are calculated via the dispersion in each axis. The error is composed of two parts: 1, the spatial and velocity resolutions; 2, the *S/N* ratio. Normally, the total error is dominated by the spatial and velocity resolutions that typically contribute an error of ∼40%.

[b] The rotation temperature is the average value in each clump. The uncertainties are composed of the statistic errors and the systematic errors. The systematic errors (generally 30%) are higher than the statistic errors (<10%) when the average rotation temperature is low, while the statistic errors (generally 20%) are higher than systematic errors (<10%) when the average rotation temperature is high. For clumps that do not have detectable emission in the (2, 2) line, we compute an upper limit of rotation temperature assuming that the flux density of the (2, 2) line equals to the 3σ level.